

Drift and diffusion of paraexcitons in Cu_2O : Deformation-potential scattering in the low-temperature regime

D. P. Trauernicht* and J. P. Wolfe

Department of Physics and Materials Research Laboratory, University of Illinois at Urbana-Champaign, 1110 West Green Street, Urbana, Illinois 61801

(Received 2 January 1986)

The diffusion constant and drift mobility of paraexcitons in Cu_2O have been determined by the use of time-resolved luminescence imaging. Extremely large diffusion constants ($D \approx 1000 \text{ cm}^2/\text{s}$) and drift mobilities ($\mu \approx 10^7 \text{ cm}^2/\text{eV s}$) are measured at 1.2 K. Both D and μ exhibit very rapid and unusual temperature dependences which vary with applied stress. Calculations described here show that these properties can be attributed to the novel character of paraexcitons in Cu_2O . Under zero stress this exciton is expected to couple mainly to longitudinal-acoustic phonons, which have a rather large velocity ($\approx 4.5 \times 10^5 \text{ cm/s}$). Due to the large excitonic mass ($m^* \approx 3m_0$), the thermal velocity $[(3k_B T/m^*)^{1/2}]$ of the paraexcitons at $T \lesssim 3 \text{ K}$ is slower than this sound velocity, causing a freeze-out of the phonon-emission process. A rapid increase in scattering time is expected as the temperature is lowered further, which is in agreement with the data at zero or low stress. As stress is applied, the paraexciton wave function is altered, allowing a coupling to the transverse-acoustic phonons, which have a velocity ($\approx 1.2 \times 10^5 \text{ cm/s}$) smaller than the exciton thermal velocity. Transverse-phonon emission thus reduces the exciton mobility and produces a more nearly $T^{-3/2}$ dependence, as predicted for deformation-potential scattering in the high-temperature limit. We believe that these are the first observations of the low-temperature regime of deformation-potential scattering.

I. INTRODUCTION

Since the conception of the exciton, its expected ability to transport energy over large distances (compared with atomic dimension) has proven to be quite difficult to demonstrate experimentally. Diffusion over micrometer distances has been observed in molecular crystals where the excitons are predominantly of the Frenkel type,¹ i.e., with their wave functions localized to one molecule. Typical diffusion constants are of the order $10^{-3} \text{ cm}^2/\text{s}$ at $T=300 \text{ K}$. In insulators, exciton migration has been invoked to explain transport of energy between defects,² although resonant energy transfer by photons is a competing process in these crystals. In the case of most direct-gap semiconductors, the lifetime of the excitons is so short ($\leq 1 \text{ ns}$) that they decay before moving macroscopic distances. Also, it is difficult to distinguish between the particlelike motion of excitons and the photonlike resonant energy transfer from one portion of the crystal to another. Exciton migration over large distances has been observed, however, in *indirect-gap* semiconductors, where the recombination times are much longer.³

Measurement of the drift mobility of excitons in the indirect-gap semiconductor (Si) was made by Tamor and Wolfe.⁴ Since excitons are electrically neutral, an externally applied stress gradient was necessary to provide the motive force. Tamor and Wolfe measured a standard $T^{-3/2}$ temperature dependence for the mobility over a wide range of low temperatures (1.5–30 K), indicative of acoustic deformation-potential scattering.⁵ The absence of impurity scattering was attributed to the neutrality of the exciton (a bound electron-hole pair) and the high puri-

ty of the Si crystal. The mobility is related to the exciton-phonon scattering time by the relation $\mu = \tau/m^*$, where m^* is the translational effective mass. A completely different experimental method for measuring excitonic scattering times is the transient-grating method, which has been applied to CuCl by Aoyagi *et al.*⁶ Also, Zinov'ev *et al.*⁷ recently reported diffusion-constant measurements in CdS .

In this paper we present a study of the transport of paraexcitons in the *direct-gap* semiconductor Cu_2O at low temperatures. A stress-gradient method similar to that used in Ref. 4 is employed to measure the drift mobility of paraexcitons. Also, the diffusion constant is measured under zero applied stress. The results are quite remarkable. Diffusion constants $\approx 1000 \text{ cm}^2/\text{s}$ and mobilities $\approx 10^7 \text{ cm}^2/\text{eV s}$ were measured at $T=1.2 \text{ K}$. These numbers indicate that the paraexciton has an immense ballistic mean free path of $\sim 70 \mu\text{m}$. In addition, both parameters, D and μ , exhibited temperature dependences deviating from the usual deformation-potential prediction. They were also found to be dependent on the externally applied stress. This suggests an unusual situation in which the deformation potential (gap shift divided by strain) is stress dependent. By comparison, exciton drift mobilities in Si and Ge show no evidence of a stress dependence.

Cu_2O provides a unique system in which to study excitonic phenomena. It exhibits a classic Rydberg series [$E_n = (2.173 - 0.097/n^2) \text{ eV}$] in absorption due to the formation of excitons.⁸ There are actually four exciton series observed: the so-called yellow, green, blue, and violet series associated with different conduction and valence bands. The $n=1$ yellow exciton line, studied in this work,

is the lowest-lying state and has been extensively studied.⁹ It displays only a very weak absorption and does not fit the above Rydberg series formula. Specifically, its binding energy is ≈ 140 meV, compared to the Rydberg, 97 meV, describing the $n \geq 2$ excited energy levels of the yellow series. For photoexcitation at low temperatures, the $n=1$ level is effectively the only state occupied.

Because the conduction- and valence-band extrema are doubly spin degenerate $^2\Gamma_6^+$ and $^2\Gamma_7^+$ states, respectively, the $n=1$ exciton level actually consists of two components, given by $^2\Gamma_6^+ \times ^2\Gamma_7^+ = ^3\Gamma_{25}^+ + ^1\Gamma_2^+$. The $^3\Gamma_{25}^+$ orthoexciton (triply degenerate) and the $^1\Gamma_2^+$ paraexciton (singly degenerate) are energetically split by an exchange interaction, with the paraexciton lying lower in energy by about 12 meV. By symmetry, direct optical creation or recombination of an orthoexciton is quadrupole allowed (no phonon involved) while the paraexciton transition is highly forbidden. Both orthoexcitons and paraexcitons are observable via the emission of a photon and an appropriate parity optical phonon. Under the application of a uniaxial stress, the no-phonon line of the paraexciton also becomes visible.¹⁰

The forbiddenness of the orthoexciton and paraexciton transitions is because Cu_2O is centrosymmetric (i.e., parity is a good quantum number) and both the conduction and valence bands have positive parity;¹¹ therefore, a dipole transition involving creation or annihilation of an exciton in an even-parity angular-momentum state is forbidden. Hence, the recombination time of these excitons should be long. The orthoexciton lifetime is shortened by conversion to the lower-lying paraexciton state.^{12,13} The paraexciton, however, should be long lived. Generally, orthoexciton and paraexciton lifetimes in synthetically grown Cu_2O are observed to be a few nanoseconds.¹³ But, recently, in naturally grown crystals of Cu_2O , a very long paraexciton lifetime has been reported.¹² Our experiments are performed on samples cut from these same naturally grown crystals. At temperatures below 4.2 K we measure a paraexciton lifetime $\tau_1 \approx 0.5 \mu\text{s}$. This lifetime is long enough to allow macroscopic motion and, hence, we are able to measure the drift mobilities and diffusion constants of paraexcitons in Cu_2O . The highly forbidden nature of the paraexciton transition precludes the resonant transfer of energy by emission and reabsorption of photons; hence the motion of excitons is particlelike.

To explain the anomalous temperature- and stress-dependent mobilities, we are forced to reexamine the usual acoustic deformation-potential theory for carriers in semiconductors. We find that, due to the relatively large exciton mass and slow sound speed, the usual high-temperature approximations are not valid. Specifically, when the velocity of an exciton is below the sound velocity, phonon emission is impossible, thus inhibiting the scattering process at low temperatures. Also, the deformation-potential coupling of paraexcitons to transverse phonons is postulated to be stress dependent. By accounting for the proper low-temperature exciton-phonon kinetics and modeling the shear deformation potential from static-stress data, we can explain all of the anomalous transport properties of paraexcitons in Cu_2O .

This paper is organized as follows: In Secs. II and III

the experimental techniques and the measurements of excitonic diffusion constants are described. In Sec. IV we deal with the low-temperature limit of deformation-potential scattering and present a theoretical estimate of the diffusion constant. In Sec. V the experimental measurements of exciton mobilities are described, followed in Sec. VI by an explanation of the stress-dependent mobilities.

II. EXPERIMENTAL DETAILS

The experiments were performed on three samples cut from the same naturally grown crystal mentioned above. All three were regular parallelepipeds with two (100) faces and four (110) faces. One sample was never stressed and was used to measure the diffusion constant under zero applied stress. Its dimensions were $1.9 \times 2.0 \times 2.8 \text{ mm}^3$ with the long dimension along a $\langle 100 \rangle$ axis. Another sample had dimensions $1.5 \times 1.5 \times 1.5 \text{ mm}^3$ and was used to measure the mobility under the highest applied stress. The third sample measured $1.8 \times 2.4 \times 3.0 \text{ mm}^3$, with the long dimension along a $\langle 100 \rangle$ axis. This crystal was used to obtain the majority of the mobility results. This sample's larger cross-sectional area did not allow us to obtain as large a stress in the center portion of the sample as with the smaller-cross-sectional-area sample. The stressing arrangement will be explained in Sec. V A.

To measure the transport properties of excitons, we use the technique of time-resolved luminescence imaging. This technique has been proven very useful in studying the motional behavior of excitonic matter in indirect-gap semiconductors.¹⁴ The essential ingredients in this method are a highly polished crystal to allow one to determine the spatial origin of the luminescence, a high-quality lens to produce a magnified image of the sample, and some type of image-translation capability (to be described below). Time resolution is achieved by use of standard photon-counting techniques.

A block diagram of our experimental setup is shown in Fig. 1. A cw argon-ion laser pumps a dye laser which is cavity-dumped. R6G dye permitted wavelength tunability over a (580–630)-nm range. The cavity-dumped pulse has approximately 15 ns full width at half maximum. A portion of this pulse energy was directed toward a photodiode, which provided a monitor of the pulse stability on an oscilloscope as well as a trigger for the detection circuitry. The main portion of the laser beam is directed toward the sample through a 105-mm focal-length lens. Luminescence is collected in a direction perpendicular to the laser beam. The luminescence collection lenses are high-quality multielement camera lenses with variable apertures. The light emerging from the lenses is passed through a pair of scanning mirrors (with orthogonal rotation axes) and focused onto the entrance slit of a spectrometer, thus providing a real, magnified image of the sample that can be translated in two dimensions. These scanning mirrors are front-surface mirrors mounted on precision galvanometers in a configuration which minimizes image distortion.

A spectrometer with a 1-m focal length and a 1200-(grooves/mm) grating was used when high spectral resolution was required. This spectrometer (Spex Industries

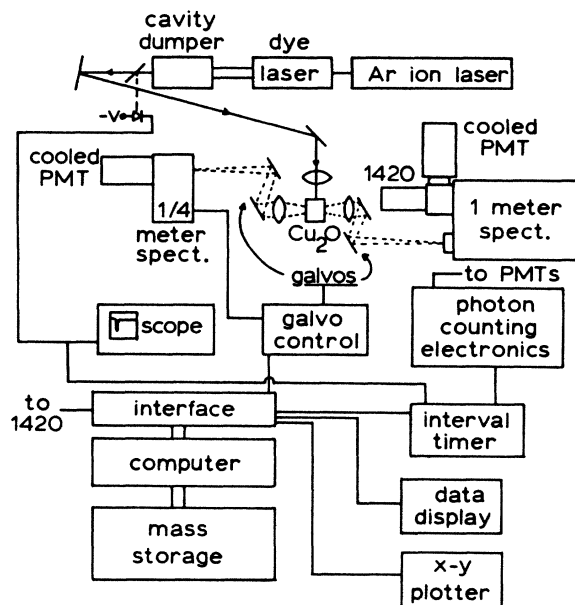


FIG. 1. Block diagram of the experimental setup for time-resolved luminescence imaging of Cu_2O . See the text for an explanation of the system.

model 1704) was equipped with a dual-exit-port assembly allowing two means of detection: (1) an intensified silicon diode array detector (Princeton Applied Research model 1420), and (2) a cooled photomultiplier tube (RCA 31034A) for photon counting. A special spectrometer with lower dispersion ($\frac{1}{4}$ m focal length, 1200 grooves/mm grating) was used for mobility measurements, where the photon energy depended on spatial position due to the strain gradient. The grating in this spectrometer was mounted on a galvanometer which was controlled by the computer, as described in detail below. A cooled photomultiplier tube, of the same type as above, was used with this $\frac{1}{4}$ -m spectrometer.

Time resolution was provided by an interval timer designed and built in our laboratory. This device times the arrival of a photon after a trigger pulse by counting the number of 100-MHz-clock pulses which occur between the trigger and the photocurrent pulse. The times of arrival of up to 16 photons could be recorded after a particular laser pulse, but on the average the count rates were less than one photon per laser pulse. We chose to operate with 20 ns resolution which was quite adequate for these experiments. A microcomputer, which controls the experiment, reads the interval timer and creates a histogram of arrival times.

An extremely efficient method of data collection is to record an entire luminescence decay curve (histogram) for each value of another control parameter. For example, to measure the diffusion constant of excitons in an unstrained crystal, one records luminescence decay curves for, say, 128 different spatial positions in the crystal. Once this two-dimensional array is recorded, it is possible to "play back" the spatial profile of the luminescence at

any given delay time. Alternatively, one could determine the time-resolved luminescence spectra at a given spatial position by having the computer step the spectrometer wavelength after each decay curve has been recorded.

III. MEASUREMENT OF THE DIFFUSION CONSTANT

The equation governing the diffusion of finite-lived particles is assumed to be the standard diffusion equation with the addition of a term due to the finite lifetime of the particles,

$$\frac{\partial n}{\partial t} = D\nabla^2 n - \frac{n}{\tau_l}, \quad (1)$$

where $n = n(\mathbf{r}, t)$ is the particle density, τ_l is the lifetime, and D is the diffusion constant of the particles. The solution of Eq. (1), which is a δ function at $t=0$ and $\mathbf{r}=\mathbf{0}$ is, in three dimensions,

$$n(\mathbf{r}, t) \propto \frac{1}{(4\pi Dt)^{3/2}} \exp\left[-\frac{r^2}{4Dt}\right] \exp\left[-\frac{t}{\tau_l}\right]. \quad (2)$$

Since the intensity of luminescence is proportional to the density of particles, Eq. (2) also describes the spatial and temporal dependence of the emitted luminescence intensity.¹⁵ One sees that the spatial distribution is a Gaussian whose width changes with time. Defining Δ as the full width at half maximum of this Gaussian, one can easily show that

$$\Delta^2(t) = 2.77(4Dt). \quad (3)$$

Therefore, if one resolves in time the spatial profile of an initially narrow packet of excitons and extracts Δ at different delay times, the slope of Δ^2 versus t will yield the diffusion constant. This method effectively eliminates the lifetime τ_l from the problem. The fact that the initial distribution created by the laser has some finite size (i.e., not a true δ function in space) does not present a serious problem. If the initial distribution is nearly Gaussian in shape, the subsequent distributions will be the same as those for a δ -function source at some earlier time.

The excitation configuration we chose was to create a fine vertical line of excitons *inside* the crystal away from any perturbing surfaces [see inset of Fig. 2(a)]. This is accomplished by adjusting the wavelength of the dye laser to give a very long absorption length: the photon energy is tuned to the low-energy edge of the phonon-assisted orthoexciton absorption band, thus creating an orthoexciton and a 110-cm^{-1} optical phonon. The orthoexcitons quickly down-convert to paraexcitons.¹³ The cylindrical expansion perpendicular to the excitation line is theoretically described by a Gaussian with Δ also given by Eq. (3).

By scanning a $4\times$ -magnified image of the sample across a rectangular aperture of the spectrometer (vertical slit, $250\ \mu\text{m}$; horizontal slit, 2 mm) and spectrally selecting the 87-cm^{-1} optical-phonon replica of the paraexciton, we obtain one-dimensional spatial profiles ("slit scans") of the emitted luminescence. Representative spatial profiles at $T=2\ \text{K}$ for successive delay times t after the peak of the laser pulse are shown in Fig. 2(a). The

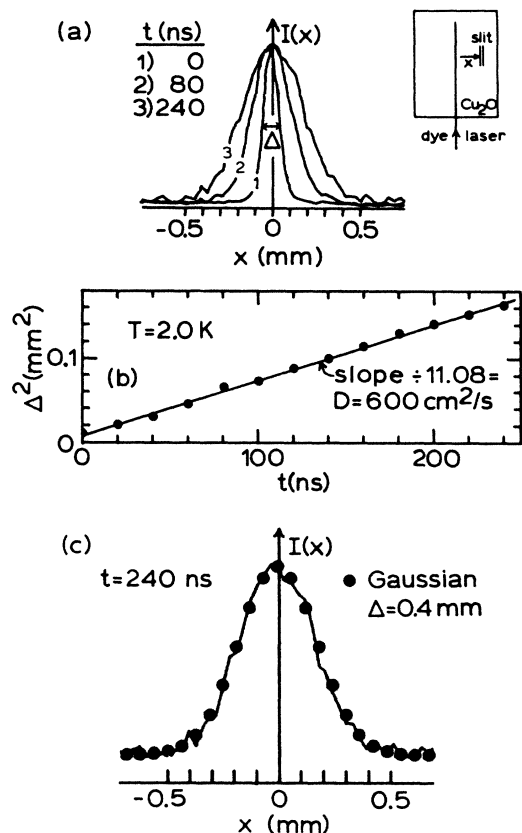


FIG. 2. (a) Time-resolved spatial profiles of paraexciton luminescence at $\lambda \approx 616.5$ nm. The data are normalized to the same peak intensity to show the growth of the full width at half maximum Δ with time. The inset shows the excitation configuration. (b) Plot of Δ^2 versus time t , after the 15-ns laser pulse, showing a linear dependence indicative of a diffusive transport. The slope of the line yields the diffusion constant as shown. (c) Gaussian fitted to the $t = 240$ ns data.

data are normalized to the same peak value. Figure 2(b) is a plot of Δ^2 versus t showing a linear dependence indicative of diffusive transport. The diffusion constant is extracted from the slope of this curve. The spatial profile of exciton luminescence is well described by a Gaussian function, as shown in Fig. 2(c).

The time-resolved expansion of paraexcitons was observed for various temperatures between 1.2 and 35 K. For $T \leq 4.2$ K, the sample was immersed in liquid helium and the temperature was varied by changing the vapor pressure of ^4He gas above the liquid. For temperatures greater than 4.2 K, the sample was vapor-cooled in a Janis Super-Varitemp cryostat. A calibrated carbon resistor mounted near the sample was used to monitor the temperature. The average incident laser power was kept low (≤ 0.1 mW absorbed) to avoid the possibility of heating effects. High-resolution phonon-assisted luminescence spectra were also taken at these higher temperatures. Theoretical fits to the spectra assuming a Maxwell-Boltzmann distribution yielded an exciton temperature

within 0.5 K of that determined by the carbon-resistor thermometer. Two such fits are shown in Fig. 3(a); the excellent agreement of the data with the standard $E^{1/2}e^{-E/k_B T}$ form indicates that the excitons are behaving energetically as a classical gas. These spectra represent an integration over all time. Time-resolved spectra were recorded at higher excitation levels (at low T) and the spectral distribution of paraexcitons is described by the lattice temperature for all observation

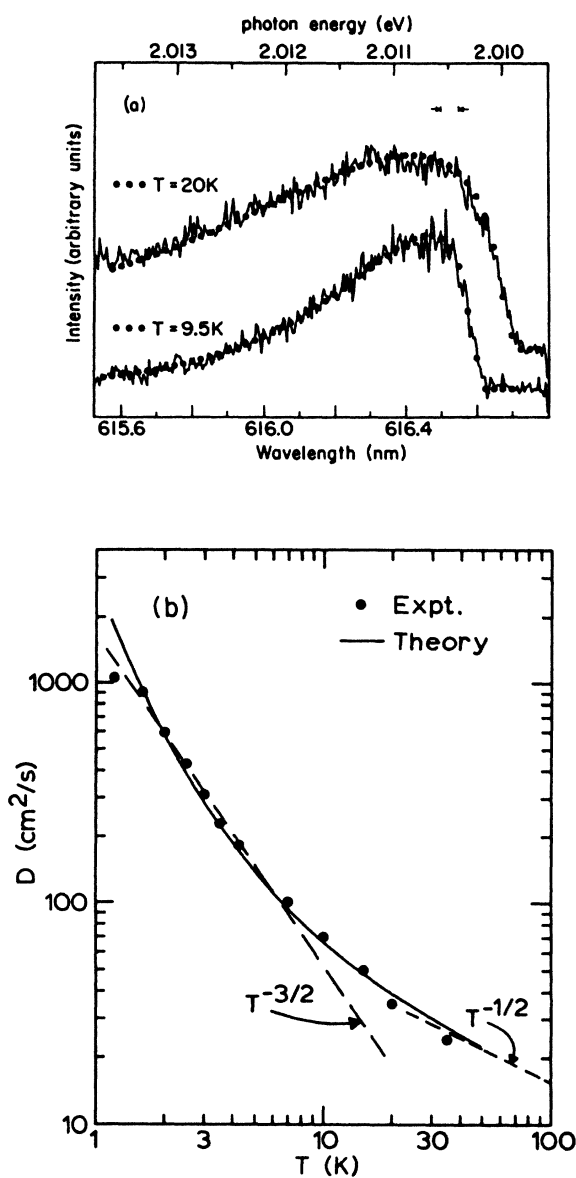


FIG. 3. (a) Time-integrated paraexciton phonon-assisted line shapes. The solid dots are Maxwell-Boltzmann distributions $E^{1/2}\exp(-E/k_B T)$ using the temperatures indicated. The theoretical curves have been convolved with the instrumental slit function. The spectra are shifted vertically for clarity. The red shift of the low-energy edge of the 20-K spectrum is due to the temperature dependence of the band gap. (b) Temperature dependence of the measured diffusion constant D for paraexcitons. The $T^{-3/2}$ dashed line is for reference, showing that there is a significant deviation from a $T^{-1/2}$ dependence. The derivation of the solid theory curve is explained in the text.

times after the end of the laser pulse.

The temperature dependence of the diffusion constant is shown in Fig. 3(b). At low temperatures, very large values of D are measured, e.g., $D \approx 1000 \text{ cm}^2/\text{s}$ at $T = 1.2 \text{ K}$. Also, the temperature dependence is very rapid, indicating phonon rather than impurity scattering. Exactly what temperature dependence does one expect for exciton-phonon scattering? At these low temperatures, the phonons with which the excitons scatter are acoustic phonons which couple through the deformation-potential interaction. The standard acoustic deformation-potential result is that the mobility μ varies as $T^{-3/2}$. If this were true here, the Einstein relation,¹⁶ $D = \mu k_B T$, implies that $D \sim T^{-1/2}$. The prediction is not in good agreement with the data of Fig. 3(b), which show a more rapid ($\sim T^{-3/2}$) dependence at temperatures below $\sim 6 \text{ K}$. This apparent anomaly will be addressed in the next section.

The large diffusion constants have interesting microscopic implications. Consider the value $D \approx 1000 \text{ cm}^2/\text{s}$ at $T = 1.2 \text{ K}$. From the Einstein relation, this value corresponds to $\mu \approx 10^7 \text{ cm}^2/\text{eV s}$. Multiplying by the exciton mass,¹⁷ $m^* = 3m_0$ (where m_0 is the free-electron mass), we calculate the mean scattering time $\tau = m^* \mu \approx 17 \text{ ns}$. By comparison, this is an order of magnitude larger than τ measured for excitons in high-purity Si.⁴ We can obtain the mean free path between scattering events, l , by multiplying τ by the thermal velocity $(3k_B T/m^*)^{1/2}$ and obtain $l \approx 70 \mu\text{m}$ at $T = 1.2 \text{ K}$. This is an enormous ballistic mean free path—about 10^5 lattice sites.

We will conclude below that these results are consistent with the weak exciton-phonon scattering rates expected for Cu_2O paraexcitons at low temperatures. The large D 's imply that exciton scattering from impurities must also be extremely weak. This fact was not too surprising for ultrapure Si, but at the outset the absence of impurity scattering seems quite fortuitous for our naturally grown materials. We can roughly estimate the impurity limit implied by our results. First, we recognize that ionized-impurity scattering should be greatly reduced because the exciton is neutral. Also, at low temperatures the impurities are not thermally ionized. Thus the exciton-impurity interaction is between two neutral species—possibly a van der Waals-type interaction which drops off as R^{-6} with dipole-dipole separation R . If the scattering cross section is of order a^2 , with $a \approx 10 \text{ \AA}$ the Bohr radius, then a scattering length $l \approx 1/n_i a^2$ is expected, where n_i is the density of scattering centers. For $l \geq 70 \mu\text{m}$, this implies $n_i \leq 10^{16} \text{ cm}^{-3}$. Unfortunately, we do not have a direct measure of the type or concentration of impurities in our samples. We do know from the relatively long paraexciton lifetime that the defect concentration must be considerably lower than that in currently available synthetic crystals.

IV. THEORETICAL ESTIMATE OF THE DIFFUSION CONSTANT

To understand these large diffusion constants, let us first consider the usual derivation of acoustic deformation-potential scattering of carriers in semiconductors.^{5,18} One begins by calculating the scattering rate,¹⁹

$$\frac{1}{\tau(\mathbf{k})} = \frac{2\pi}{\hbar} \sum_{\mathbf{q}} |M_{\mathbf{k},\mathbf{q}}|^2 \delta(E(\mathbf{k} \mp \mathbf{q}) - E(\mathbf{k}) \pm \hbar v_l q), \quad (4)$$

where $M_{\mathbf{k},\mathbf{q}}$ is the matrix element for scattering from an initial state with wave vector \mathbf{k} and energy $E(\mathbf{k})$ to a final state with wave vector $\mathbf{k} \mp \mathbf{q}$ and energy $E(\mathbf{k} \mp \mathbf{q})$ along with the emission (upper sign) or absorption (lower sign) of a phonon with wave vector \mathbf{q} and energy $\hbar v_l q$. Only longitudinal phonons (with velocity v_l) couple to the carriers in the one-valley, spherical-band approximation. The matrix element is

$$|M_{\mathbf{k},\mathbf{q}}|^2 = \frac{\hbar \mathcal{D}^2 q}{2\rho V v_l} \times \begin{cases} N_q + 1 & \text{for } \mathbf{k} - \mathbf{q} \text{ (emission)}, \\ N_q & \text{for } \mathbf{k} + \mathbf{q} \text{ (absorption)}, \end{cases} \quad (5)$$

where $N_q = [\exp(\hbar v_l q/k_B T) - 1]^{-1}$ is the Planck distribution function for the phonons, ρ is the mass density of the crystal, V is the crystal volume, and \mathcal{D} is the deformation potential (the strength of the interaction).

The coupling of carriers to phonons arises from the band shift with strain, i.e., the deformation potential. To first order, transverse (shear) waves only act to split degeneracies. Since both the conduction and valence bands in Cu_2O are orbitally nondegenerate, there should be no coupling of electrons and holes to transverse phonons in the unstressed crystal.

Utilizing the properties of the δ function, we obtain

$$\frac{1}{\tau(\mathbf{k})} = \frac{\mathcal{D}^2 m^*}{4\rho v_l \hbar^2 k} \left[\int_{L_1}^{L_2} \frac{q^2}{\exp(\hbar v_l q/k_B T) - 1} dq + \int_0^{L_3} \frac{q^2}{1 - \exp(-\hbar v_l q/k_B T)} dq \right]. \quad (6)$$

The limits of integration $L_{1,2,3}$ depend on the carrier wave vector. There are two distinct wave-vector regions of interest: (1) $k < m^* v_l / \hbar$ and (2) $k > m^* v_l / \hbar$. If $k < m^* v_l / \hbar$, then only the first integral (due to phonon absorption) is nonzero and has limits

$$L_1 = 2[(m^* v_l / \hbar) - k] \quad \text{and} \quad L_2 = 2[(m^* v_l / \hbar) + k].$$

If $k > m^* v_l / \hbar$, then $L_1 = 0$, L_2 is unchanged, and the second integral (due to phonon emission) has the limit $L_3 = 2[k - (m^* v_l / \hbar)]$.

For most carrier systems, acoustic-phonon scattering is not observable at low temperatures because impurity scattering dominates. Thus, the high-temperature approximation, $\hbar v_l q \ll k_B T$, is generally assumed. This simplifies the integrands. Also, at all but the lowest temperatures, the thermal velocity of the carriers greatly exceeds the sound velocity; hence, the majority of k vectors are much larger than $m^* v_l / \hbar$. This is equivalent to the statement that the energy of the carrier is much larger than the energy of the scattered phonon; therefore, the carrier-scattering events are nearly elastic. This then simplifies the limits of the above integrals: $L_1 = 0$, $L_2 = L_3 = 2k$. Under these approximations, the rates of absorption and emission of phonons are equal, and the scattering rate for a given k vector reduces to

$$\frac{1}{\tau(k)} = \frac{\mathcal{D}^2 m^* (k_B T)}{\pi \hbar^3 \rho v_l^2} k. \quad (7)$$

To obtain the mobility μ , one averages over the carrier distribution,²⁰

$$\mu = \frac{1}{m^*} \frac{\langle E(\mathbf{k})\tau(k) \rangle}{\langle E(\mathbf{k}) \rangle}, \quad (8)$$

where $\langle \rangle$ denotes a thermal average. The final result is⁵

$$\mu = \frac{2(2\pi)^{1/2} \hbar^4 \rho v_l^2}{3 \mathcal{D}^2 (m^*)^{5/2}} (k_B T)^{-3/2}, \quad (9)$$

which is the standard result in the high-temperature approximation. The diffusion constant is related to the mobility through the Einstein relation, $D = \mu k_B T$. This implies a $T^{-1/2}$ behavior for D .

For carriers at low temperatures, the validity of the above assumptions must be reconsidered.²¹ Basically, the thermal energy of the particles is very small, and thus the energy of the phonon cannot be ignored in the scattering process. The principal idea is contained in Fig. 4, which characterizes the scattering process in one dimension. The energy of the particle is $(\hbar k)^2/2m^*$. By emitting a phonon, a particle with initial wave vector k_4 can scatter to a state with wave vector k_1 . The phonon emitted is represented as the line connecting the two states. The slope of the line is the velocity of the phonon, v_l . Similarly, a particle in the state labeled k_3 can scatter into k_2 . However, if the initial wave vector is less than $k_c^l = m^* v_l / \hbar$, there is no final state which allows conservation of energy and momentum. This "cutoff" corre-

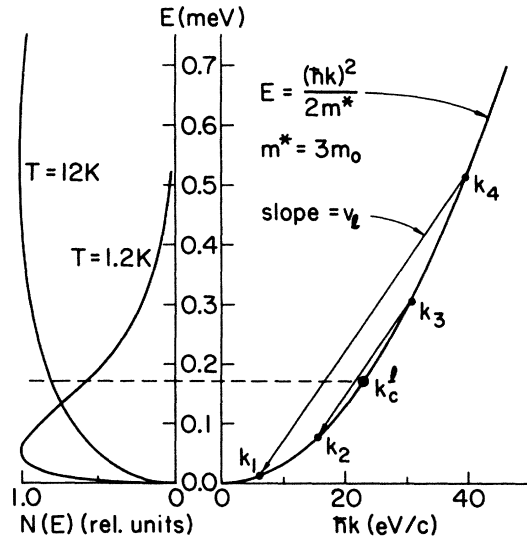


FIG. 4. Energy versus momentum, $\hbar k$, for the paraexciton (mass $= 3m_0$) and normalized Maxwell-Boltzmann distributions, $N(E) \propto E^{1/2} \exp(-E/k_B T)$, at 1.2 and 12 K. The sloped lines represent phonon-emission scattering events. For initial k values less than k_c^l , longitudinal-phonon emission is forbidden by energy and momentum conservation. At 1.2 K, this region of forbidden phonon-emission contains a significant fraction of the total number of particles, whereas at 12 K this region does not.

sponds to the wave vector of a particle with velocity equal to the sound velocity. Particles with velocity less than v_l cannot emit a phonon.

Consider now the thermal distribution of particles shown on the left-hand side of Fig. 4. At high temperatures there is a broad distribution of particle energies so that those particles with velocity less than v_l constitute a small fraction of the total number of particles. This low-energy regime is justly ignored in the high-temperature calculation. However, at low temperatures the distribution is much narrower in energy and the number of particles with velocity less than v_l is now a significant fraction of the total number and cannot be ignored in the calculation.

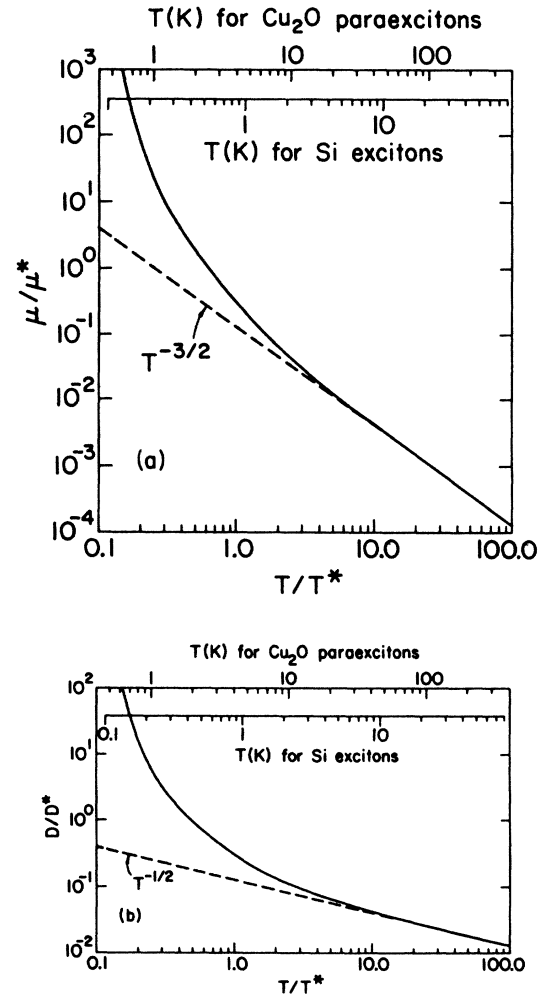


FIG. 5. (a) Theoretical normalized mobility μ/μ^* versus T/T^* , where $\mu^* \equiv 16\sqrt{2\pi} \hbar^4 \rho / [3 \mathcal{D}^2 (m^*)^4 v]$ and $T^* \equiv m^* v^2 / k_B$. The numerical calculation used Eqs. (6) and (8) with no high-temperature approximations. The top scale is the temperature appropriate for paraexcitons in Cu₂O. The lower scale is the temperature appropriate for excitons in Si assuming $m^* = 0.45m_0$ and $v \approx 5.4 \times 10^5$ cm/s, an average transverse-phonon velocity. We use the transverse velocity because excitons in Si can scatter from transverse phonons at zero applied stress. (b) Similar plot for the diffusion constant using the above calculation of mobility and the Einstein relation $D = \mu k_B T$. $D^* \equiv 16\sqrt{2\pi} \hbar^4 \rho v / [3 \mathcal{D}^2 (m^*)^3]$.

TABLE I. Parameters and characteristic temperatures for excitons in selected semiconductors.

Material	m^*/m_0	v_t (10^5 cm/s)	v_l (10^5 cm/s)	T_l^* (K)	T_t^* (K)
Cu ₂ O	3.0 ^a	1.2 ^b	4.5 ^b	0.3	4.0
Si	0.45 ^c	5.4 ^d	9.0 ^d	0.9	2.4
Ge	0.21 ^c	3.3 ^d	5.3 ^d	0.2	0.4
GaAs	0.69 ^c	3.1 ^e	5.1 ^e	0.4	1.2

^aReference 17.

^bReference 23. Also, see text.

^cS. M. Kelso, Phys. Rev. B **25**, 7631 (1982). The sum of the electron and hole transverse masses in the infinite stress limit was used. $\langle 100 \rangle$ stress for Si and $\langle 111 \rangle$ stress for Ge.

^dH. B. Huntington, *The Elastic Constants of Crystals* (Academic, New York, 1958). The program mentioned in Ref. 39 was used and an average over the symmetry directions was done.

^eSadao Adachi, J. Appl. Phys. **58**, R1 (1985). For the exciton mass, the sum of the electron and heavy hole masses was used. To obtain the phonon velocities, the program mentioned in Ref. 39 was used and an average over the symmetry directions was done.

A numerical solution of Eqs. (6) and (8) with no high-temperature approximations is given in Fig. 5(a). Temperature is plotted in units of $T^* = m^*v^2/k_B$, where T^* is a characteristic temperature of the low-temperature regime, and v is the appropriate phonon velocity ($v = v_l$ for unstrained Cu₂O). The mobility is plotted in units of $\mu^* \equiv 16\sqrt{2\pi}\hbar^4\rho/3\mathcal{D}^2(m^*)^4v$, which equals the high-temperature mobility [Eq. (9)] evaluated at $T = T^*/4$. For $T \gg T^*$ the expected $T^{-3/2}$ dependence is obtained. At temperatures below T^* the temperature dependence is considerably more rapid. Figure 5(b) shows the corresponding diffusion constant, obtained from the Einstein relation. The top of both plots indicates the temperature scale appropriate to paraexcitons in Cu₂O. The curve in Fig. 5(b) is also shown as the solid line in Fig. 3(b). The only fitting parameter used was an overall multiplier. Other parameters needed in the calculation were extracted from the literature or reference books: $\rho = 6$ g/cm³, $m^* = 3m_0$ for the $1s$ exciton,^{17,22} and the average longitudinal-phonon velocity²³ $v_l = 4.5 \times 10^5$ cm/s (elastic isotropy assumed in the calculation). Considering the overall multiplier to give a dynamic deformation potential for the exciton, this would yield $\mathcal{D} = 1.2$ eV. (This value is not far from the band-gap hydrostatic deformation potential of 2.1 eV quoted in Ref. 32.)

This observation of the low-temperature regime in acoustic deformation-potential scattering relies upon the large mass of the paraexciton and the fact that it interacts much more strongly with longitudinal phonons than transverse phonons. From the excellent agreement between experiment and theory [Fig. 3(b)], we conclude that the steep temperature dependence of D below about 6 K is due to the freeze-out of longitudinal-phonon emission by the excitons and the rapid decrease in phonon occupation number N_q . The transverse phonons in Cu₂O have a sound velocity about 4 times lower, implying that the emission freeze-out for these phonons would occur at a temperature 16 times lower than for longitudinal phonons. If the paraexcitons were strongly coupled to the transverse phonons, the rapid dependence of D in the experimental temperature range would not have occurred.

To illustrate the effect of exciton mass and phonon velocity, we list in Table I some calculated characteristic temperatures T^* for excitons in other crystals.

V. MEASUREMENT OF THE MOBILITY

A. Experimental aspects

To determine the mobility of particles, a known force F is applied and their resultant drift velocity v_d is measured. Because excitons are electrically neutral, we cannot use an electric field to provide the motive force. However, since the exciton energy decreases with increasing stress (see Fig. 11), a stress gradient produces an effective force on these particles.

An inhomogeneous stress was applied by pressing a rounded plunger (section of a glass lens with radius of curvature either 1.6 or 2.5 cm) against a flat surface of the sample. This Hertzian geometry creates a maximum of shear stress inside the sample below the plunger-sample contact area. Figure 6(a) shows a schematic of the stress distribution inside the crystal. The solid lines represent "equipotentials," or curves of constant exciton energy. Details of this stress method have been previously reported for indirect-gap semiconductors.²⁴

The energy gradient is determined by selectively tuning the dye laser to the locally down-shifted orthoexciton quadrupole resonance. Typically, the orthoexcitons are created few hundred micrometers directly below the shear-stress maximum (SSM), and their drift path is straight upwards.

In order to calibrate the applied force on the excitons, one must measure the change in potential energy U of the excitons along the drift path, giving $F = -dU/dz$. This is accomplished by collecting spectra at different positions along the drift path, as shown in Fig. 6(b). The bottom spectrum is collected from the SSM under an applied stress which is comparable to the stress the excitons experience at the beginning of their drift path for the data to be described. For this spectrum, the laser was tuned to the low-energy edge of the (strain-shifted) phonon-assisted

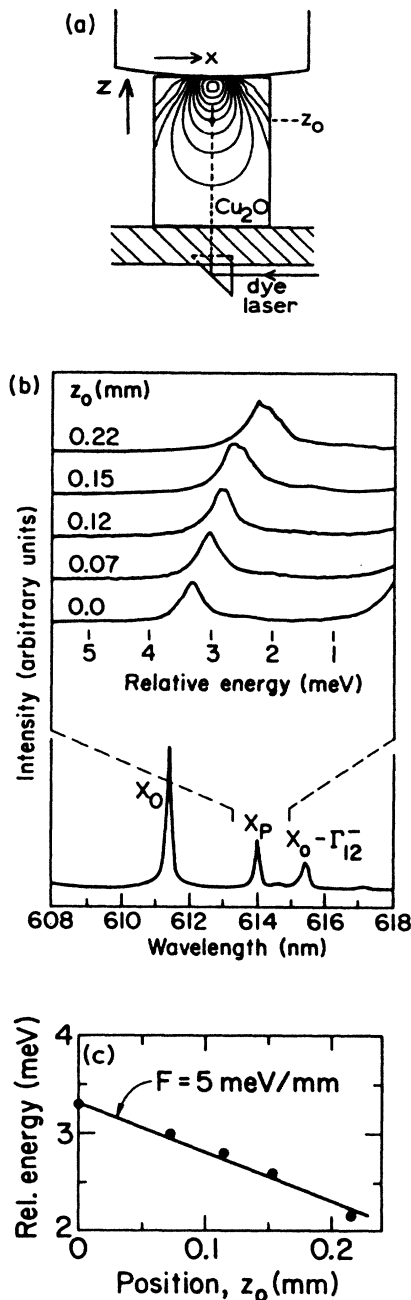


FIG. 6. (a) Schematic of the stressing arrangement used to provide the motive force for the measurement of mobility. The curves inside the crystal are schematic "equipotential" curves, or curves of constant exciton energy. There is a maximum of shear stress created inside the sample. The excitons are attracted to this shear-stress maximum (SSM). They are created at position z_0 by resonant excitation of the orthoexciton line and subsequent down-conversion to paraexcitons. (b) Luminescence spectra for different excitation regions in the crystal, as controlled by the laser wavelength. Luminescence is collected directly from the excitation point z_0 . The shifts in these spectra are used to calibrate the applied motive force, as explained in the text. X_0 is the orthoexciton no-phonon line, X_p is the paraexciton no-phonon line, and $X_0-\Gamma_{12}$ is the 110-cm^{-1} optical-phonon replica of the orthoexciton. (c) Paraexciton energy versus pump position z_0 . The negative of the slope of the line gives the average motive force F applied to the excitons.

orthoexciton absorption. Three luminescence lines are identified. The intense line labeled X_0 is due to no-phonon orthoexciton recombination and $X_0-\Gamma_{12}$ is a phonon-assisted orthoexciton line. The line labeled X_p is the no-phonon paraexciton, which is observable under a symmetry-lowering stress.^{10,25} It is the energy position of this paraexciton line which we want to determine as a function of position along the drift path. In order to produce a localized packet of excitons, the no-phonon orthoexciton quadrupole line was resonantly pumped. Since this is locally a very sharp resonance, only a very small region of the crystal is excited, namely, that where the strain-shifted orthoexciton energy and the laser photon energy are the same. (Due to this resonant excitation, there is also a significant amount of resonantly Raman scattered light,⁹ causing, for example, the $X_0-\Gamma_{12}$ line to greatly increase in intensity.) The photoproduced orthoexcitons rapidly down-convert to paraexcitons via processes which have not been clearly identified.¹³

The expanded spectra in Fig. 6(b) show the paraexciton line for different excitation positions (as controlled by the laser wavelength) along the drift path. These spectra were taken with the 1-m spectrometer and the diode array detector. For a given excitation wavelength, the position of excitation was determined by recording "vertical" slit scans (described below) using the $\frac{1}{4}$ -m spectrometer. Either orthoexciton or paraexciton luminescence was selected; both have maximum intensity at the pumped spot. Shown in Fig. 6(c) is a plot of the shift of the paraexciton energy as a function of pump position, z_0 , along the drift path. The average force is the slope of this curve.

To measure the drift velocity v_d , the motion of the paraexcitons is time-resolved after their creation at a particular position, z_0 . Again, after the vertical dimension, z , is scanned because the excitons are moving upward toward the SSM. To accomplish this, a configuration of three mirrors (two mounted on galvanometers) rotated the image by 90° , so that vertical motion inside the crystal resulted in horizontal motion across the entrance slit of the spectrometer. This allowed a spatial integration of the light in a plane perpendicular to the drift direction.

Because the wavelength of the emitted light changes with spatial position, it is necessary to scan the spectrometer grating simultaneously with the image translation. The angle of the $\frac{1}{4}$ -m spectrometer grating was voltage controlled, as described previously. By applying proportional voltages to the respective galvocontrollers, the image mirror and grating were synchronously scanned. The wavelength range was adjusted so that the wavelength of the paraexciton luminescence peak tracked the corresponding spatial position.

Figure 7(a) shows some time-resolved slit scans obtained in this manner. The time delay between the displayed scans is 80 ns. The data are characterized by a center-of-mass motion of the exciton packet (due to drift) and a broadening of the distribution (due to diffusion). To determine the drift velocity, we plot in Fig. 7(b) the peak position (the center of the packet) as a function of time. The slope is the drift velocity.

Given the measured quantities F and v_d , the mobility μ is v_d/F . Our initial approach was to measure the drift ve-

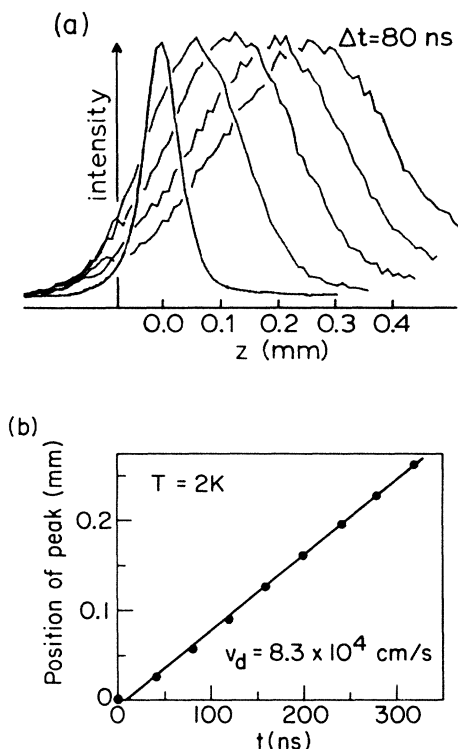


FIG. 7. (a) Time-resolved spatial profiles of paraexciton luminescence showing the drift due to the application of the motive force determined in Fig. 6(c). The peak intensities are normalized for clarity. The effective time gate is 20 ns. The spreading in the width of the profiles is due to exciton diffusion. (b) Position of the peak of the exciton distribution as a function of time. The slope yields the drift velocity v_d . With the motive force measured in Fig. 6(c), F , and this v_d , we determine the mobility $\mu = v_d/F = 1.7 \times 10^6 \text{ cm}^2/\text{eV s}$ for this temperature and applied stress. The average applied stress in the drift region is $\bar{\sigma} = 2.1 \text{ kbar}$, as determined from Fig. 11 and the spectral shift of the paraexciton luminescence.

locities for several calibrated forces in order to show that v_d scaled with F . We obtained a paradoxical result: as F was increased, the drift velocity did not increase proportionally, suggesting that mobility was *force* dependent. Actually, we were discovering that the mobility for paraexcitons in Cu_2O was *stress* dependent. To increase the force on the excitons we applied more pressure to the crystal, which also increased the average stress in the measurement region of the crystal.²⁶ Thus, in the measurements described below it was necessary to record both the stress gradient (force) and the mean stress in the drift region. For a given drift measurement the variation in total stress was only about 25%.

To measure the temperature dependence of μ , it was not necessary to measure F at each temperature because the pressure on the crystal was unchanged. F was typically measured at 2 K. The incident energy per pulse was approximately 20 nJ and the pulse repetition rate was 40 kHz. The absorbed energy was actually a very small fraction of the incident energy because the absorption of the quadrupole line occurs only in a region of the crystal less than 0.1 mm in length. The size of this excitation region

is determined by the local stress gradient and the spectral width of the laser line ($\sim 0.05 \text{ nm}$). A significant amount of this “absorbed” light is resonantly Raman scattered; hence, only a small initial density of excitons is created, which we estimate to be less than 10^{15} cm^{-3} .

B. Results

Figure 8 shows the temperature dependence of the mobility for $T \leq 4.2 \text{ K}$, i.e., with the sample immersed in liquid helium. Mobility measurement above 4.2 K was difficult because the drift velocities were low and the excitons did not drift very far during their lifetime. The different data sets are for different applied crystalline stresses. The parameter $\bar{\sigma}$ is the average applied stress over the traversed distance and is determined from the spectral energy position of the paraexciton line E_{para} near the midpoint of travel. The conversion of E_{para} to $\bar{\sigma}$ is determined from previous uniform-stress experiments.^{25,27}

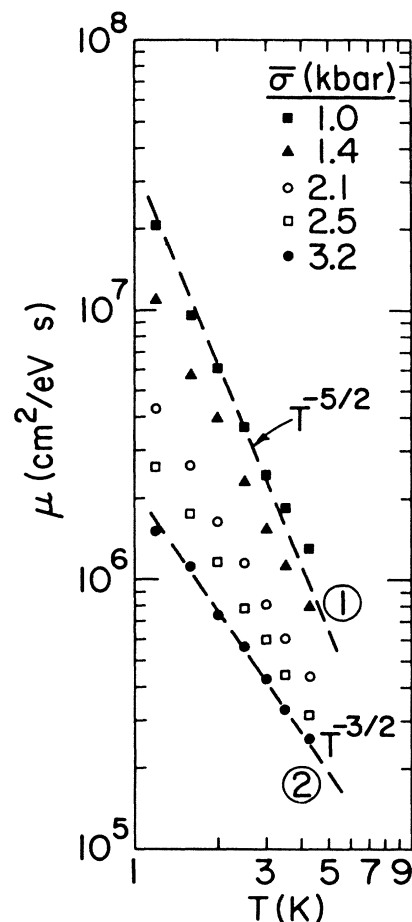


FIG. 8. Temperature dependence of the measured drift mobility of paraexcitons. The five sets of data are for different applied stresses. The $T^{-5/2}$ dashed line (marked 1) and the $T^{-3/2}$ dashed line (marked 2) are for reference to show the change in the temperature dependence of μ . The applied motive forces were 0.01 eV/cm (\blacksquare), 0.02 eV/cm (\blacktriangle), 0.05 eV/cm (\circ), 0.08 eV/cm (\square), and 0.11 eV/cm (\bullet).

(See Fig. 11.) The data in Fig. 8 indicate that both the absolute value of the mobility and its temperature dependence vary with the applied stress.

First consider the lowest-stress data—the black solid squares corresponding to $\bar{\sigma}=1$ kbar. The measured drift mobilities, e.g., $\mu \approx 2 \times 10^7$ $\text{cm}^2/\text{eV s}$ at $T=1.2$ K, are indeed as high as implied by the previous diffusion constants. Also, the temperature dependence of μ is reasonably consistent with the rapid temperature dependence of D for $T \leq 4.2$ K. The relation $D \sim T^{-3/2}$ and the Einstein relation imply $\mu \sim T^{-5/2}$, which is shown by the dashed line marked 1; however, $\mu k_B T$ is about a factor of 2 larger than D measured for the unstressed crystal.

Considering all the data sets in Fig. 8, as $\bar{\sigma}$ is increased, there is a continuous decrease in μ as well as a gradual modification of the temperature dependence.²⁸ The mobilities for the highest stress follow a nearly $T^{-3/2}$ behavior (line marked 2).

Before a model is proposed to explain these results, there is one additional parameter that can be extracted from this drift data: a diffusion constant can be measured from the spreading of the packet of excitons in the direction of motion. The full width at half maximum Δ of the distribution should be given by Eq. (3), while the center of the Gaussian packet moves with velocity v_d . Diffusion constants obtained from the drift data are plotted in Fig. 9. The same general trends are seen in these data, i.e., a decrease in D with increasing stress and also a change in the temperature dependence.

The lines marked 1 and 2 in Fig. 9 are derived from those correspondingly marked in Fig. 8 with the use of the Einstein relation. The extracted diffusion constants do lie within the range predicted by $\mu k_B T$. At the lower stresses even the absolute magnitudes of D and $\mu k_B T$ are

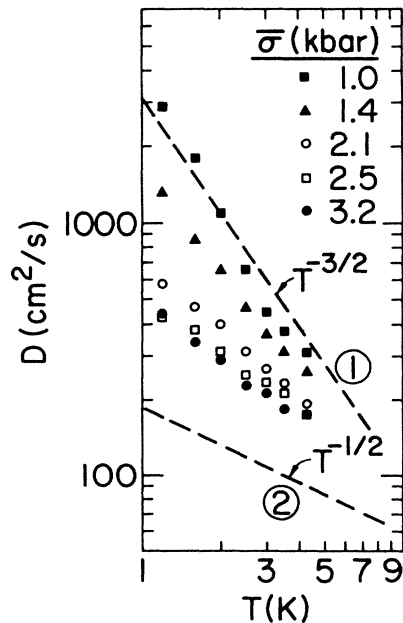


FIG. 9. Temperature dependence of the extracted diffusion constant from the drift data. The dashed lines labeled 1 and 2 correspond to the similarly labeled lines in Fig. 8, as related by the Einstein relation $D = \mu k_B T$.

in good agreement. However, strict agreement with the Einstein relation does not seem to hold at higher stresses. There is some uncertainty in extracting D from the drift data because the forces applied to the excitons are not perfectly constant over the measured path; the force increases somewhat as the excitons approach the SSM, which would tend to make the packet spread more rapidly and hence cause an *overestimate* of the diffusion constant. Also, the intensity of the direct paraexciton line is stress dependent,^{25,29} increasing in intensity at higher applied stress, which could affect the shape of the exciton luminescence distribution. However, it is not clear how to make this correction properly, and we chose to analyze the raw data making no *ad hoc* intensity corrections. Along these lines, we note that at low applied stress we found good correspondence between mobilities measured with spectral selection of the phonon-assisted paraexciton line and those obtained using the no-phonon line with no attempted intensity corrections.

VI. PROPOSED EXPLANATION OF THE STRESS-DEPENDENT MOBILITIES

What could cause the mobility to decrease with increasing stress? An increased coupling of excitons and acoustic phonons with applied stress implies that the deformation potential is getting larger. If the coupling to longitudinal phonons alone increased with stress, the mobility would decrease, but the temperature dependence would remain unchanged because the deformation potential is simply an overall multiplier in the scattering rate. If, however, the coupling to transverse phonons changed with stress, this could have a major effect on the temperature dependence of μ because the characteristic temperature T_t^* associated with transverse-phonon scattering is much lower than T_l^* . This is because the transverse-phonon velocity v_t is nearly a factor of 4 less than the longitudinal velocity v_l in Cu_2O . Specifically, the value²³ of v_t varies between 1.14×10^5 and 1.4×10^5 cm/s , whereas the average value of v_l is about 4.5×10^5 cm/s at low temperatures. Figure 10 shows the energy E versus $\hbar k$ for the paraexciton and the left-hand side shows a $T=1.2$ K Maxwell-Boltzmann distribution. (This is an expanded version of Fig. 4.) Longitudinal-phonon emission is forbidden for exciton wave vectors below the cutoff value, $k_c^l \equiv m^* v_l / \hbar$, as previously discussed. However, transverse-phonon emission is forbidden for wave vectors below $k_c^t \equiv m^* v_t / \hbar$, a much smaller value. Thus, even for a low temperature of 1.2 K only a very small fraction of the total number of particles have their emission process frozen out. One would expect, then, that the scattering rate will more closely resemble the high-temperature situation, where the temperature dependence of μ is $T^{-3/2}$. This dependence is close to that observed at higher stresses, indicating the presence of transverse-phonon scattering.

We now consider how the transverse phonons can become the dominant scattering source for paraexcitons under an applied stress. A clue lies in the highly nonlinear dependence of paraexciton energy on stress as

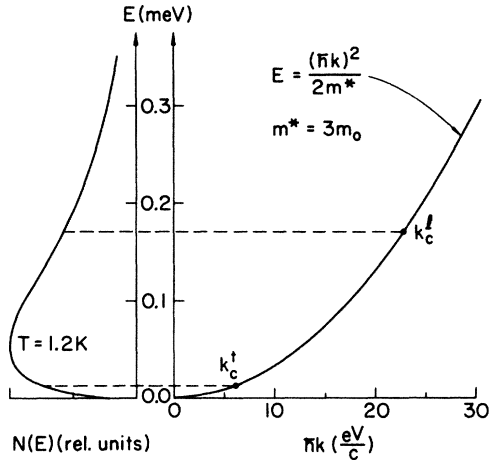


FIG. 10. Expanded version of Fig. 4. The cutoff value of k below which longitudinal-phonon emission is forbidden is k_c^l , and the cutoff wave vector for transverse-phonon emission is k_c^t , a much smaller value. The number of particles with forbidden longitudinal-phonon emission is much larger than the number with forbidden transverse-phonon emission.

shown in Fig. 11. By comparison, excitons in Si display a linear shift in energy with applied stress.³⁰ The slope of the E -versus- σ curve is closely related to the deformation potential. Exciton mobilities in Si show no evidence of a stress dependence.⁴

A basic question concerning exciton-phonon scattering is whether the phonon scatters separately with the electron and hole, or with both as a unit, i.e., how is the excitonic deformation potential related to those of the electron and hole? For the temperatures in our experiments, the thermal phonons have wavelengths much larger than the excitonic Bohr radius (~ 10 Å); thus, the electron and hole feel the same local deformation and should scatter as a unit. Therefore, we expect that the shift of the paraexciton energy with static stress gives an indication of its coupling to phonons.

Waters *et al.*³¹ recently measured the stress dependence of the exciton energies of the yellow series in Cu_2O , excluding the $n=1$ paraexciton state, for uniform uniaxial stress in a $\langle 100 \rangle$ direction. They also reported a theoretical analysis of their results. Shortly afterwards, Trebin *et al.*³² carried out a more exact theoretical treatment of the problem. Both theories give virtually identical results if expanded to the same order of approximation. We will use the second order perturbation results of Waters *et al.*, which are easily adaptable to our purposes.

According to deformation-potential theory, the coupling of phonons to carriers is caused by the modulation of the energy band of the carriers by the strain of the phonon. To first order in strain, the strength of the interaction, the deformation potential, is determined by the band shift per unit strain. For a nondegenerate spherical band in a cubic semiconductor, only dilational strains cause the band to shift in energy. This can be easily seen by expanding the energy modulation ΔE to first order in strain in the following manner:^{5,18}

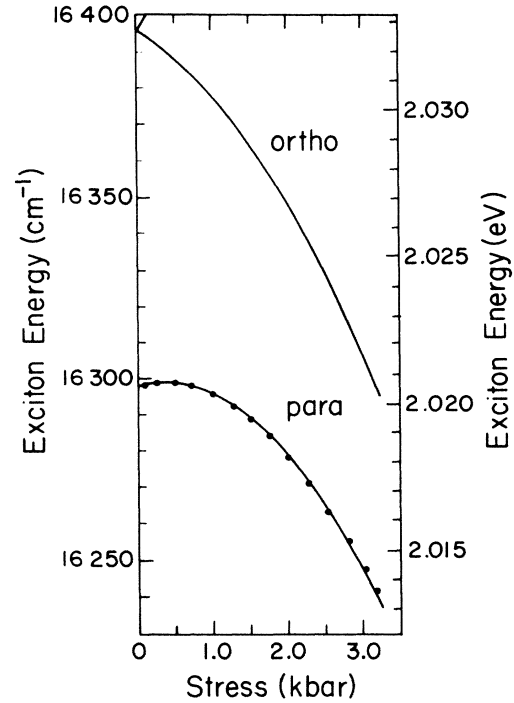


FIG. 11. Energy of the orthoexciton and paraexciton as a function of applied $\langle 100 \rangle$ uniaxial stress σ . The orthoexciton curves plotted are from Ref. 31 and used with our measurement of orthoexciton energy shift to calibrate the applied stress. With simultaneous measurement of the spectral shift of the paraexciton, we determine its energy versus applied stress. The solid curve through the data is fitted to the curve $E_{\text{para}} = A + B\sigma - C\sigma^2$, with $A = 16298 \text{ cm}^{-1}$, $B = 4.96 \text{ cm}^{-1} \text{ kbar}^{-1}$, and $C = 7.36 \text{ cm}^{-1} \text{ kbar}^{-2}$.

$$\Delta E = \alpha_{xx}\epsilon_{xx} + \alpha_{yy}\epsilon_{yy} + \alpha_{zz}\epsilon_{zz} + \alpha_{zy}\epsilon_{zy} + \alpha_{xz}\epsilon_{xz} + \alpha_{xy}\epsilon_{xy}, \quad (10)$$

where ϵ_{mn} are the components of the strain tensor and α_{mn} are coefficients of expansion. Since the system has cubic symmetry, ΔE is unaffected by reflections through planes perpendicular to the x , y , or z axes. ϵ_{mn} for $m \neq n$ changes sign upon reflection through planes perpendicular to the m or n axis; therefore, $\alpha_{mn} = 0$ for $m \neq n$. Also, the x , y , and z axes are all equivalent in a cubic system; therefore, $\alpha_{xx} = \alpha_{yy} = \alpha_{zz} = \mathcal{D}_d$. This now gives the familiar result^{5,18}

$$\Delta E = \mathcal{D}_d(\epsilon_{xx} + \epsilon_{yy} + \epsilon_{zz}) = \mathcal{D}_d \text{Tr} \vec{\epsilon}. \quad (11)$$

Using $\epsilon_{mm} \equiv \partial u_m / \partial x_m$ with u_m the m th component of the local displacement from equilibrium,³³ and $u_m = u_0 p_m e^{i(\mathbf{q} \cdot \mathbf{r} - \omega t)}$ with u_0 the amplitude of the phonon, p_m the m th component of the polarization vector, \mathbf{q} the wave vector, and ω the frequency of the phonon, one obtains $\epsilon_{mm} = u_m q_m$. Therefore, $\epsilon_{xx} + \epsilon_{yy} + \epsilon_{zz} = \mathbf{u} \cdot \mathbf{q}$ and only longitudinal phonons (with $\mathbf{u} \parallel \mathbf{q}$) couple to the carriers. The matrix element is given by Eq. (5).

We can explicitly see that only dilational strains affect the paraexciton energy to first order by considering the strain Hamiltonian and paraexciton wave function con-

structed by Waters *et al.*³¹ The strain Hamiltonian

$$H_{st} = a \text{Tr} \vec{\epsilon} - 3b \left[(L_z^2 - \frac{1}{3} L^2) \epsilon_{zz} + \text{c.p.} \right] - 2d \sqrt{3} (\{L_y, L_z\} \epsilon_{yz} + \text{c.p.}), \quad (12)$$

where L_m are angular-momentum operators, c.p. means cyclic permutations, $\{L_y, L_z\} = L_y L_z + L_z L_y$, and a , b , and d are band deformation potentials.^{31,34} The wave function they give for the paraexciton is

$$\phi_p = \frac{1}{\sqrt{12}} [(Y_2^{-2} - Y_2^2)(\alpha\beta_c + \beta\alpha_c) + 2Y_2^{-1}\beta\beta_c - 2Y_2^1\alpha\alpha_c],$$

where Y_l^m are the spherical harmonics, α (β) is spin “up” (“down”) for the hole, and α_c (β_c) is spin “up” (“down”) for the electron. In the calculation of $\langle \phi_p | H_{st} | \phi_p \rangle$, the only nonzero contribution, regardless of the form of the strain $\vec{\epsilon}$, is from the $a \text{Tr} \vec{\epsilon}$ term. Since transverse phonons have no dilational character (in an isotropic medium), there is no coupling (or very weak coupling) of paraexcitons to transverse phonons at zero applied stress. This is consistent with the zero-stress diffusion-constant results, which were explained solely by longitudinal-phonon coupling.

Considering the application of a $\langle 100 \rangle$ stress, Waters *et al.* showed that the dependence of the paraexciton energy, through second order in perturbation theory, is of the form

$$E_{\text{para}} = A + B\sigma - C\sigma^2, \quad (13)$$

where σ is the magnitude of the uniform uniaxial $\langle 100 \rangle$ stress. The source of each term is easily identified. The constant A is the unperturbed zero-stress energy. The $B\sigma$ term comes from the dilational term $a \text{Tr} \vec{\epsilon}$, where $\text{Tr} \vec{\epsilon} = (S_{11} + 2S_{12})\sigma$ and S_{mn} are elastic compliance constants.³³ $C\sigma^2$ is due to a term of lower symmetry in H_{st} , namely the second term in Eq. (12). The last term in Eq. (12) does not contribute for stress along a fourfold axis.

Figure 11 shows a fit of Eq. (13) to the experimental paraexciton shift under an applied $\langle 100 \rangle$ stress. Both orthoexciton and paraexciton luminescence were collected from the SSM. The spectral shift of the orthoexciton was used to calibrate the local stress, using the uniform stress data of Waters *et al.* The fit of Eq. (13) to the data is excellent and the resulting parameters A , B , and C are given in the caption. The dominance at high stress of a term such as $C\sigma^2$, which incorporates the effects of shearing strains, is also verified by the fact that paraexcitons collect, and thus have an energy minimum, at a shear-stress maximum.³⁵

Now consider the effect of a phonon when a static uniaxial stress $\bar{\sigma}$ is applied to the crystal in a $\langle 100 \rangle$ direction. Let an additional $\langle 100 \rangle$ stress due to the phonon be $\Delta\sigma$. Substituting $\sigma = \bar{\sigma} + \Delta\sigma$ into Eq. (13) and ignoring terms second order in $\Delta\sigma$, we find

$$E_{\text{para}} = A' + B(\Delta\sigma) - 2C\bar{\sigma}(\Delta\sigma), \quad (14)$$

where A' contains all terms not involving $\Delta\sigma$. To first order in $\Delta\sigma$, there is a modulation of the paraexciton en-

ergy from the third term in Eq. (14), which is associated with strains other than pure dilation. Therefore, when $\bar{\sigma}$ is nonzero, a transverse phonon can couple to the paraexciton. The amplitude of energy modulation is linearly dependent on the applied stress $\bar{\sigma}$. This implies a deformation potential linearly dependent on $\bar{\sigma}$. We have oversimplified the problem by ignoring phonon-induced stresses in directions other than the applied stress, but we believe the result to be qualitatively correct for the more general case: i.e., a given shear wave will have a deformation potential linearly dependent on the magnitude of static stress. Also, we are ignoring the nonuniformity of our applied stresses. In the regions of the crystal “below” the SSM where the excitons travel, this should not be a major oversight because the stresses are reasonably uniform perpendicular to the travel direction, and do not vary significantly ($\leq 25\%$) along the travel direction.

A qualitative understanding of this stress-dependent transverse-phonon coupling can be gained by considering the band structure¹¹ of Cu₂O. Ignoring spin, the conduction band is nondegenerate, and the valence band would be threefold degenerate in the absence of spin-orbit interaction. With spin-orbit coupling, the valence band splits into an upper singly degenerate band (ignoring a spinlike degeneracy) associated with the yellow exciton series and a lower doubly degenerate band associated with the green exciton series. This ordering of the valence bands is opposite the case of Si or GaAs.³⁶ Since the spherical band extrema in Cu₂O are nondegenerate, they are unaffected to first order in shear stress. The lower, degenerate valence band is split by shear stress and this band will mix with the upper valence band as stress is applied. This mixing causes the upper valence band to couple to shear waves as static stress is applied.

From Raman scattering, Yu and Shen^{17,37} determined that the orthoexciton in Cu₂O interacts with longitudinal phonons 7 times more strongly than with transverse phonons. The orthoexciton is a threefold-degenerate state which has a linear splitting under the application of a symmetry-lowering stress. This splitting is due to a combination of exchange and strain via mixing with the green series^{31,32,38} (associated with the lower doubly degenerate band). Exchange has no effect on the paraexciton; hence, to first order there is no shift in energy due to a symmetry-lowering stress. We believe that this means orthoexcitons are more strongly coupled to transverse phonons than paraexcitons at zero applied stress, even though the orthoexcitons are still weakly coupled. We have not measured the transport properties of orthoexcitons because of their much shorter lifetime.

In order to calculate the momentum-damping time, we must express the energy modulation due to a phonon in terms of strain. An applied uniaxial stress (chosen to be along the z axis) lowers the crystal symmetry. From arguments similar to those used in obtain Eq. (11), the paraexciton energy shift is given by

$$\Delta E = \alpha_{xx}(\epsilon_{xx} + \epsilon_{yy}) + \alpha_{zz}\epsilon_{zz}. \quad (15)$$

We define in the conventional way^{18,20} the components of a deformation potential, $\mathcal{D}_d = \alpha_{xx}$ and $\mathcal{D}_u = \alpha_{zz} - \alpha_{xx}$. Equation (15) then becomes

$$\Delta E = \mathcal{D}_d \text{Tr} \bar{\epsilon} + \mathcal{D}_u \epsilon_{zz}, \quad (16)$$

and \mathcal{D}_u is the shear component of the deformation potential, which, by the above arguments, is linearly dependent on applied stress $\bar{\sigma}$.

The form of the scattering matrix elements depends on the polarization of the phonons involved. We assume elastic isotropy, which greatly simplifies the calculation, and makes the two transverse modes degenerate. Using a coordinate system with the polar axis along the stress direction (+z direction), let one transverse mode have polarization pointing in the direction of increasing polar angle θ , and the other pointing in the direction of increasing azimuthal angle ϕ . The longitudinal mode is polarized in the radial direction along \mathbf{q} , the phonon wave vector. Expressing the wave vector \mathbf{q} and the three polarizations in their x, y, z components in terms of the angles θ and ϕ , and using the definition $\epsilon_{mm} = \partial u_m / \partial x_m$ and a plane-wave expression for a phonon as above, the matrix elements are now given by^{18,20}

$$|M_{\mathbf{k},\mathbf{q}}|_i^2 = \frac{(\mathcal{D}_d + \mathcal{D}_u \cos^2 \theta)^2 \hbar q}{2V\rho v_l} \times \begin{cases} N_{\mathbf{q}} & \text{for absorption,} \\ N_{\mathbf{q}} + 1 & \text{for emission,} \end{cases} \quad (17)$$

$$|M_{\mathbf{k},\mathbf{q}}|_i^2 = \frac{(\mathcal{D}_u \sin \theta \cos \theta)^2 \hbar q}{2V\rho v_t} \times \begin{cases} N_{\mathbf{q}} & \text{for absorption,} \\ N_{\mathbf{q}+1} & \text{for emission.} \end{cases}$$

Only one transverse mode couples under these assumptions, the one with polarization along increasing θ direction. Since the strongest transverse scattering occurs for $\theta = 45^\circ$ and 135° , we choose $v_t = 1.2 \times 10^5$ cm/s, which corresponds to an average slow transverse velocity at $\theta = 45^\circ$.^{23,39} Also, the mass of the paraexcitons is assumed to remain isotropic and independent of applied stress. \mathcal{D}_u , and thus the ratio $\mathcal{D}_u / \mathcal{D}_d$, is assumed to vary

linearly with applied stress, $\bar{\sigma}$.

Since our experiments are performed at low temperatures and the scattering events cannot be treated as elastic in exciton energy as previously discussed, a proper calculation of the momentum-damping time requires a complete solution of the Boltzmann equation for inelastic scattering, or alternatively a Monte Carlo simulation. These approaches are beyond the scope of our present paper. One approximate approach is to simply use Eq. (4) as we did in a preceding section. If the scattering events were elastic, Eq. (4) should be multiplied by $1 - \cos \theta'$, where θ' is the angle between the initial and final wave vectors of the scattered particles.^{18,20} This weights large-angle scattering over small-angle scattering, which is more appropriate for the momentum-damping time rather than the simple scattering time. However, since there is significant energy loss in the collisions at low temperature, the $1 - \cos \theta'$ factor is not correct and we choose to ignore it. Basically, the energy change in collision implies a momentum change. To obtain μ , we average over a Maxwell-Boltzmann distribution according to Eq. (8).

Another method we have used to determine μ is to calculate the rate of change in field-directed momentum averaged over a drifted Maxwell-Boltzmann distribution.¹⁸ Since the excitons are at relatively low density, the assumption of a drifted distribution is not completely justified; however, it provides a basis on which to gain an understanding of the physics of the problem. The rate of change in field-directed particle momentum is given by¹⁸

$$-\frac{d(\hbar k_F)}{dt} = \frac{V}{(2\pi)^3} \int d^3 q (\hbar q_F S_{\text{emission}} - \hbar q_F S_{\text{absorption}}), \quad (18)$$

where $q_F = q \cos \theta$ is the component of the wave vector in the field direction (direction of motive force) and

$$S_{\text{emission}} = \frac{(\mathcal{D}_u + \mathcal{D}_d \cos^2 \theta)^2 \hbar q}{2V\rho v_l} (N_{\mathbf{q}} + 1) \delta(E(\mathbf{k} - \mathbf{q}) - E(\mathbf{k}) + \hbar v_l q) + \frac{(\mathcal{D}_u \sin \theta \cos \theta)^2 \hbar q}{2V\rho v_t} (N_{\mathbf{q}} + 1) \delta(E(\mathbf{k} - \mathbf{q}) - E(\mathbf{k}) + \hbar v_t q), \quad (19a)$$

$$S_{\text{absorption}} = \frac{(\mathcal{D}_d + \mathcal{D}_u \cos^2 \theta)^2 \hbar q}{2V\rho v_l} N_{\mathbf{q}} \delta(E(\mathbf{k} + \mathbf{q}) - E(\mathbf{k}) - \hbar v_l q) + \frac{(\mathcal{D}_u \sin \theta \cos \theta)^2 \hbar q}{2V\rho v_t} N_{\mathbf{q}} \delta(E(\mathbf{k} + \mathbf{q}) - E(\mathbf{k}) - \hbar v_t q), \quad (19b)$$

where the proper phonon velocities must be included in the $N_{\mathbf{q}}$. Equation (18) is then averaged over the drifted Maxwell-Boltzmann distribution,

$$\exp[-(\hbar \mathbf{k} - m^* \mathbf{v}_d)^2 / 2m^* k_B T].$$

This yields the magnitude of the damping force, $F_{\text{ph}} \equiv \langle -d(\hbar k_F) / dt \rangle$, due to the phonon scattering. For a packet of particles drifting with velocity v_d , F_{ph} must balance the applied motive force and the mobility is simply v_d / F_{ph} . An advantage to this method is that it attempts to account for both momentum damping and energy loss without assuming elastic scattering. We will discuss the

results of this method below.

Of course, both of the above methods give a standard $T^{-3/2}$ dependence for the mobility at higher temperatures, and, in fact, for zero stress (i.e., longitudinal-phonon scattering only) both methods give a nearly identical temperature dependence over the entire temperature range calculated (1.2–300 K). When transverse scattering is incorporated, both methods give qualitatively similar results, the major difference being that, for a given value of $\mathcal{D}_u / \mathcal{D}_d$, the first method gives a slightly more rapid temperature dependence than the second method.

The results of the second method are shown as the solid

lines in Fig. 12. The procedure for fitting the theory to the experimental mobilities was as follows. There were only two adjustable parameters used to simultaneously fit all the data: the ratio of $\mathcal{D}_u/\mathcal{D}_d$ to $\bar{\sigma}$ and an overall multiplier. The effects of these two parameters are quite orthogonal because $\mathcal{D}_u/\mathcal{D}_d$ is determined by the spread in the data with applied stress whereas the overall multiplier simply adjusts the absolute scale of μ . Figure 12 shows that the theory accounts very well for both the variation of μ with stress and the changing form of the temperature dependence.

How reasonable are the fitting parameters? The overall multiplier can be interpreted as a calibration of the deformation potentials for this approximate theory. The result is $\mathcal{D}_d \approx 0.7$ eV. This value is about 60% the value of \mathcal{D}_d obtained in the zero-stress diffusion analysis. The ratio $\mathcal{D}_u/\mathcal{D}_d = -0.3\bar{\sigma}$ gave the best fit to the data. The negative sign indicates that dilational and shearing strains have opposing effects on the paraexciton energy. A theoretical estimate of this ratio may be obtained from a comparison of Eqs. (14) and (16). We identify the dila-

tional terms as $\mathcal{D}_d \text{Tr}\vec{\epsilon}$ and $B(\Delta\sigma)$ and the shear terms as $\mathcal{D}_u \epsilon_{zz}$ and $-2C\bar{\sigma}(\Delta\sigma)$, respectively. Using $\text{Tr}\vec{\epsilon} = (S_{11} + 2S_{12})\Delta\sigma$ and $\epsilon_{zz} = S_{11}\Delta\sigma$, we obtain the ratio

$$\mathcal{D}_u/\mathcal{D}_d = -[2C(S_{11} + 2S_{12})]/(S_{11}B)\bar{\sigma}.$$

With $B = 4.96 \text{ cm}^{-1} \text{ kbar}^{-1}$, $C = 7.36 \text{ cm}^{-1} \text{ kbar}^{-2}$ from our fit to Eq. (13) and $S_{11} = 4.169 \times 10^{-3} \text{ kbar}^{-1}$ and $S_{12} = -1.936 \times 10^{-3} \text{ kbar}^{-1}$ from Ref. 32, we obtain $\mathcal{D}_u/\mathcal{D}_d = -0.2\bar{\sigma}$. This estimate of the relative scattering strengths for shear and longitudinal waves agrees fairly well with the value $\mathcal{D}_u/\mathcal{D}_d = -0.3\bar{\sigma}$ obtained from the fit to the mobility data.

VII. CONCLUSIONS

The transport properties of paraexcitons in Cu_2O at low temperatures have been measured. The long paraexciton lifetime allowed macroscopic drift before recombination. Time-resolved luminescence imaging was used to measure the diffusion constants and mobilities for a range of temperatures and applied stresses. At zero applied stress, the temperature dependence of the diffusion constant deviated significantly from the $T^{-1/2}$ dependence which is usually thought to characterize acoustic deformation-potential scattering. Recalculating the scattering time using proper low-temperature exciton-phonon kinetics (i.e., making none of the high-temperature approximations) resulted in an excellent agreement between experiment and theory. This is the first demonstration, to our knowledge, of the low-temperature regime in acoustic deformation-potential scattering.

The strain-gradient technique was employed to provide a motive force for determination of the paraexciton drift mobility. Resonant volume excitation provided an initially small packet of excitons. The resultant mobility as well as its temperature dependence was found to be stress dependent; increasing stress resulted in a decreasing mobility as well as a less rapid temperature dependence. This effect was related to the nonlinear dependence of paraexciton energy on applied uniaxial stress. A model incorporating a stress-dependent coupling to transverse-acoustic phonons was proposed in which the shear deformation potential was assumed to vary linearly with applied uniaxial stress. Calculations incorporating this stress-dependent coupling yielded good agreement between experiment and theory.

ACKNOWLEDGMENTS

We are grateful to A. Mysyrowicz for supplying the Cu_2O crystals, for contributing to the initial discovery of high paraexciton mobility (Ref. 28), and for his continuing advice. We acknowledge a North Atlantic Treaty Organization (NATO) Travel grant which fostered this interaction. We thank K. Hess for helpful discussions. This work was supported by the U.S. Air Force Office of Scientific Research Grant No. AFOSR-84-0384. Facility support was provided by the National Science Foundation under the Material Research Laboratories Program Grant No. NFS-DMR-80-24000 and by the A. O. Beckman Research Foundation.

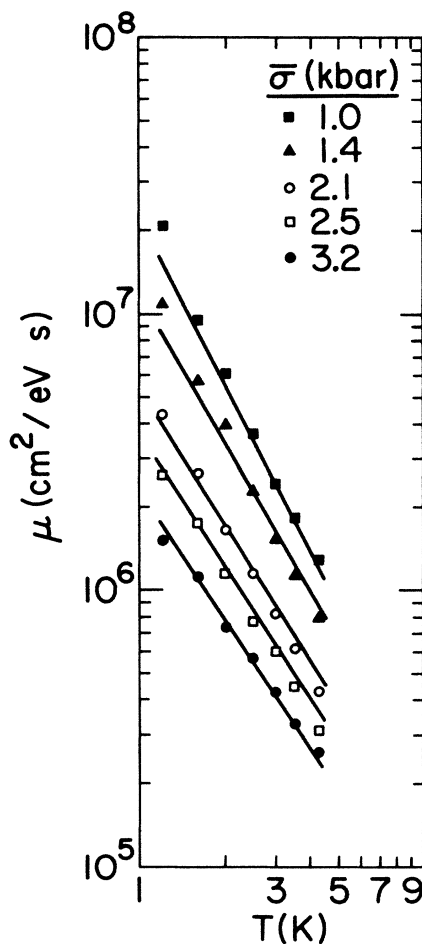


FIG. 12. Comparison of the measured paraexciton mobilities with the deformation-potential theory explained in the text. The symbols represent the experimental data and the solid lines are theory, as determined by an overall scale factor and the ratio $\mathcal{D}_u/\mathcal{D}_d = -0.3\bar{\sigma}$, as described in the text.

- *Present address: Kodak Research Laboratories, Eastman Kodak Company, 1999 Lake Avenue, Rochester, NY 14650.
- ¹See, for example, V. M. Agronovich and M. D. Galanin, *Electronic Excitation Energy Transfer in Condensed Matter*, in *Modern Problems in Condensed Matter Sciences*, edited by V. M. Agronovich and A. A. Maradudin (North-Holland, New York, 1982), Vol. 3.
- ²See, for example, Ch. B. Lushchik, in *Excitons*, in *Modern Problems in Condensed Matter Sciences*, edited by V. M. Agronovich and A. A. Maradudin (North-Holland, New York, 1982), Vol. 2. This volume contains a helpful general bibliography at the end.
- ³To our knowledge, the first experimental estimate of the exciton diffusion constant in Ge at 3 K was given by Pokrovskii [Phys. Status Solidi A 11, 385 (1972)]. A more detailed measurement at 4.2 K was made by J. C. Culbertson [Ph.D. thesis (LBL-15472), University of California at Berkeley, 1982 (unpublished)]. Studies of exciton diffusion in Si have been conducted by M. A. Tamor [Ph.D. thesis, University of Illinois at Urbana-Champaign, 1982 (unpublished)] and by F. M. Steranka and J. P. Wolfe (unpublished).
- ⁴M. A. Tamor and J. P. Wolfe, Phys. Rev. Lett. 44, 1703 (1980); Phys. Rev. B 26, 5743 (1982).
- ⁵J. Bardeen and W. Shockley, Phys. Rev. 80, 72 (1950).
- ⁶Yoshinobu Aoyagi, Yusaburo Segawa, and Susumu Namba, Phys. Rev. B 25, 1453 (1982).
- ⁷N. N. Zinov'ev, L. P. Ivanov, I. G. Lang, S. T. Pavlov, A. V. Prokaznikov, and I. D. Yaroshetskiy, Zh. Eksp. Teor. Fiz. 84, 2153 (1983) [Sov. Phys.—JETP 57, 1254 (1983)].
- ⁸For a review of general excitonic properties in Cu₂O, see, for example, V. T. Agekyan, Phys. Status Solidi A 43, 11 (1977), or S. Nikitine, in *Optical Properties of Solids*, edited by S. Nudelman and S. S. Mitra (Plenum, New York, 1969).
- ⁹Much resonant Raman scattering work has been done involving the 1s orthoexciton. See, for example, P. Y. Yu, in *Excitons*, Vol. 14 of *Topics in Current Physics*, edited by K. Cho (Springer-Verlag, New York, 1979), and references therein.
- ¹⁰The $n=1$ paraexciton state of Cu₂O was postulated to exist by R. J. Elliott (Ref. 11). The no-phonon line was first seen by E. F. Gross, F. I. Kreingold, and V. L. Makarov (Pis'ma Zh. Eksp. Teor. Fiz. 15, 383 (1972) [JETP Lett. 15, 269 (1972)]) under the application of a uniaxial stress. Their experiment showed the ortho-para splitting to be 96 cm⁻¹ rather than ~15 cm⁻¹ as estimated by Elliott.
- ¹¹R. J. Elliott, Phys. Rev. 124, 340 (1961).
- ¹²A. Mysyrowicz, D. Hulin, and A. Antonetti, Phys. Rev. Lett. 43, 1123 (1979).
- ¹³J. S. Weiner, N. Caswell, P. Y. Yu, and A. Mysyrowicz, Solid State Commun. 46, 105 (1983).
- ¹⁴J. P. Wolfe, J. Lumin. 30, 82 (1985).
- ¹⁵In an actual slit-scan experiment, one measures the integrated intensity from a thin slice of the distribution, corresponding to an integration of Eq. (2) over y and z . The remaining spatial function is $\exp(-x^2/4Dt)$, which has the same width as the density distribution.
- ¹⁶In this paper, we are using the units of cm²/eV s for the mobility, defined as drift velocity divided by the force, which is measured in units of eV/cm. To convert to an equivalent "electronic" mobility (drift velocity divided by the electric field) simply drop the "e" in eV.
- ¹⁷P. Y. Yu and Y. R. Shen, Phys. Rev. Lett. 32, 939 (1974).
- ¹⁸See, for example, K. Seeger, *Semiconductor Physics* (Springer-Verlag, New York, 1973).
- ¹⁹We do not include the usual $1-\cos\theta'$ multiplier, where θ' is the angle between the initial and final wave vectors, in the expression for two reasons: (1) In the high-temperature limit, the $\cos\theta'$ contributes nothing (i.e., $\langle \cos\theta' \rangle = 0$), and (2) The $1-\cos\theta'$ is derived for elastic scattering and we shall see that acoustic-phonon scattering at low temperatures cannot be considered elastic.
- ²⁰C. Herring and E. Vogt, Phys. Rev. 101, 944 (1956); E. M. Conwell, *High Field Transport in Semiconductors*, Suppl. 9 of *Solid State Physics* (Academic, New York, 1967).
- ²¹A. C. Redfield and J. D. Dow, Bull. Am. Phys. Soc. 29, 420 (1984).
- ²²The translation effective mass of the paraexciton is assumed to be the same as that of the orthoexciton. The mass of the $n=1$ yellow excitons is larger than the sum of the electron and hole masses ($\sim 1.7m_0$). This could be due to a partial breakdown of effective-mass theory since the exciton Bohr radius is small (~ 10 Å). See Ref. 37.
- ²³J. Berger, J. Castaing, and M. Fischer, J. Phys. (Paris) 40, Suppl. No. 11, 13 (1979); J. Hallberg and R. C. Hanson, Phys. Status Solidi 42, 305 (1970).
- ²⁴R. S. Markiewicz, J. P. Wolfe, and C. D. Jeffries, Phys. Rev. B 15, 1988 (1977); also see Ref. 30.
- ²⁵A. Mysyrowicz, D. P. Trauernicht, J. P. Wolfe, and H.-R. Trebin, Phys. Rev. B 27, 2562 (1983).
- ²⁶It is true that as the applied stress was increased, the motive force on the paraexcitons also increased. Could there be effects similar to high-field velocity saturation as found in many semiconductors? The largest motive force was 0.11 eV/cm, which is quite small. Also, the measured drift velocities were less than the longitudinal-phonon velocity. In order to get significant non-Ohmic behavior, one must push nondegenerate carriers at velocities much larger than the phonon velocity. Therefore, we rule out these effects as the explanation for the stress-dependent mobilities.
- ²⁷In order to determine σ in our experiment, we use the energy position of the down-shifted orthoexciton line as the calibrator. In Ref. 25 we used the theoretical result for the orthoexciton energy as a function of applied stress. For this paper (see Fig. 11), we use the experimentally determined orthoexciton energy as a function of applied stress (Ref. 31) because there was some difference between Refs. 31 and 32 at the higher applied stresses.
- ²⁸Previously [Phys. Rev. Lett. 52, 855 (1984)], we hypothesized that the $T^{-5/2}$ dependence of μ was due to a strain dependence of the deformation potential, $\mathcal{D} \propto \epsilon$. This hypothesis is superceded by the more detailed discussion of the deformation potential and exciton kinetics presented in this paper. Also note that the low-stress mobility data presented in the above reference was obtained for surface excitation and different drift direction. Our present work shows that the two geometries yield nearly identical results for the same stress and motive force. The volume-pump geometry allows us to probe the exciton drift at higher stresses and obtain a systematic stress dependence of the mobilities.
- ²⁹F. I. Kreingol'd and V. L. Makarov, Fiz. Tekh. Poluprovodn. 8, 1475 (1974) [Sov. Phys.—Semicond. 8, 962 (1975)].
- ³⁰P. L. Gourley and J. P. Wolfe, Phys. Rev. B 24, 5970 (1981).
- ³¹R. G. Waters, F. H. Pollak, R. H. Bruce, and H. Z. Cummins, Phys. Rev. B 21, 1665 (1980).
- ³²H.-R. Trebin, H. Z. Cummins, and J. L. Birman, Phys. Rev. B 23, 597 (1981).
- ³³See any "Solid State Physics" text; for example, Neil W. Ashcroft and N. David Mermin, *Solid State Physics* (Holt, Rinehart, and Winston, New York, 1976), Chap. 22.

- ³⁴G. L. Bir and G. E. Pikus, *Symmetry and Strain-Induced Effects in Semiconductors*, translated by P. Shelnitz, edited by D. Louvish (Keter, Jerusalem, 1974).
- ³⁵D. P. Trauernicht, A. Mysyrowicz, and J. P. Wolfe, *Phys. Rev. B* **28**, 3590 (1983).
- ³⁶See, for example, B. K. Ridley, *Quantum Processes in Semiconductors* (Clarendon, Oxford, 1982), p. 17.
- ³⁷P. Y. Yu and Y. R. Shen, *Phys. Rev. B* **12**, 1377 (1975).
- ³⁸V. A. Kiselev and A. G. Zhilich, *Fiz. Tverd. Tela* (Leningrad) **13**, 2398 (1971) [*Sov. Phys.—Solid State* **13**, 2008 (1972)].
- ³⁹Using the elastic constants of Ref. 23, we calculated the velocity and polarizations of slow and fast transverse phonons propagating at $\theta=45^\circ$ and various azimuthal angles using the program written by G. A. Northrop [*Comput. Phys. Commun.* **28**, 103 (1982)]. An average velocity of the slow transverse phonon was chosen because its polarization was very near the polarization in an isotropic medium for which there is phonon coupling.